Supplemental Information

High Efficiency Triboelectric Charge Capture for High Output Direct Current Electricity

Kaixian Li‡[a], Chuncai Shan ‡[a]*, Shaoke Fu[a], Huiyuan Wu[a], Wencong He[a], Jian Wang[a], Gui Li[a], Qianjin Mu[a], Shihe Du[a], Qionghua Zhao[a], Chenguo Hu[a]*, Hengyu Guo[a]*

[1]School of Physics, Chongqing Key Laboratory of Soft Condensed Matter Physics and Smart Materials, Chongqing University, Chongqing, 400044, P. R. China.

[2]These authors contributed equally to this work.

*Correspondence: chuncaishan@cqu.edu.cn (C. Shan); hucg@cqu.edu.cn (C. Hu); physghy@cqu.edu.cn (H. Guo).

Content

Supplementary Figures:

Supplementary Figure S16: Voltage curves of ICC-TENG with different PTFE-electrode pairs integrated.

Supplementary Figure S17: Voltage curves of charging capacitors by ICC-TENG at 30 rpm without PMC.

Supplementary Figure S18: The average power of ICC-TENG under various external loads at 30 rpm.

Supplementary Figure S19: Maximum NAIs density generated by ICC-TENG under various rotating speeds.

Supplementary Tables:

Supplementary Table S1: Comparison of output performance of DC-TENG, AC-TENG, and IDC-TENG.

Supplementary Table S2: The percentage of the breakdown charge and the residual charge of different materials in the first Contact-separation process.

Supplementary Table S3: Systematic comparison of charge and average power densities with the reported works.

Supplementary Notes:

Supplementary Note S1 The measurement method and theoretical analysis of triboelectric charge state of materials.

Supplementary Note S2: Influence of the number of PTFE-electrode pairs on the charge output of ICC-TENG under equal width conditions of PTFE.

Supplementary Note S3: Calculation process of energy conversion efficiency of ICC-TENG.
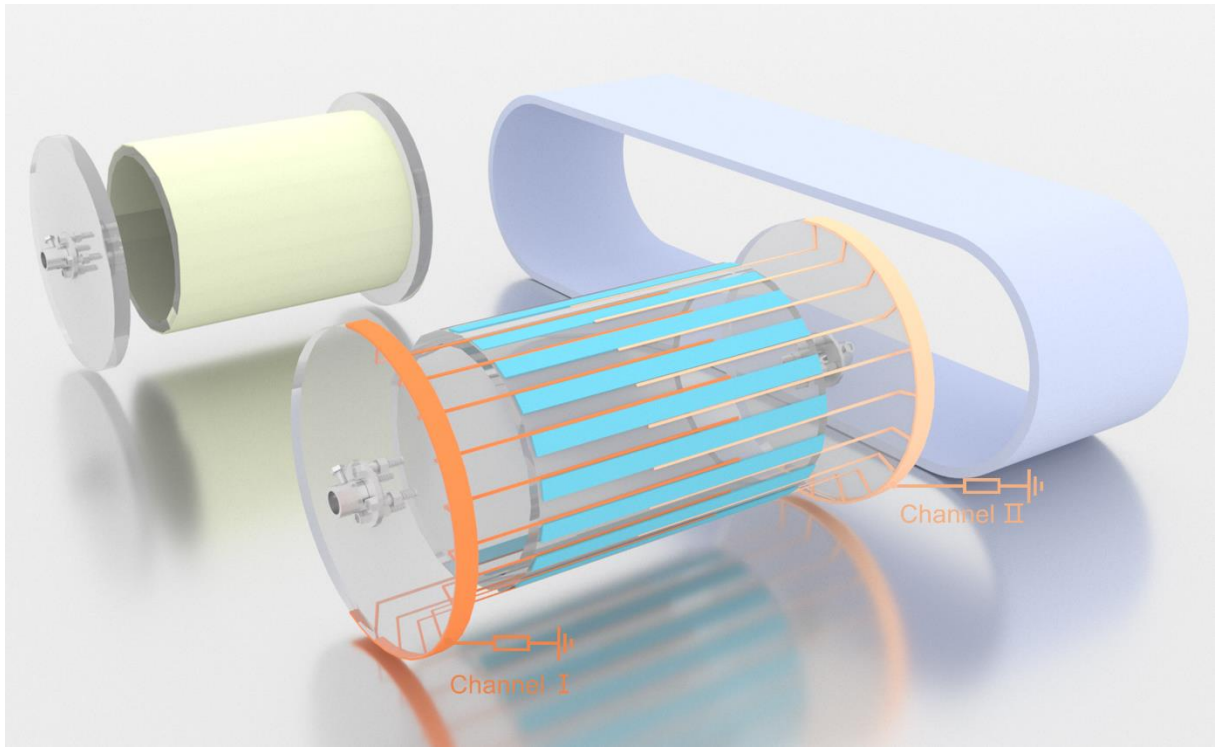
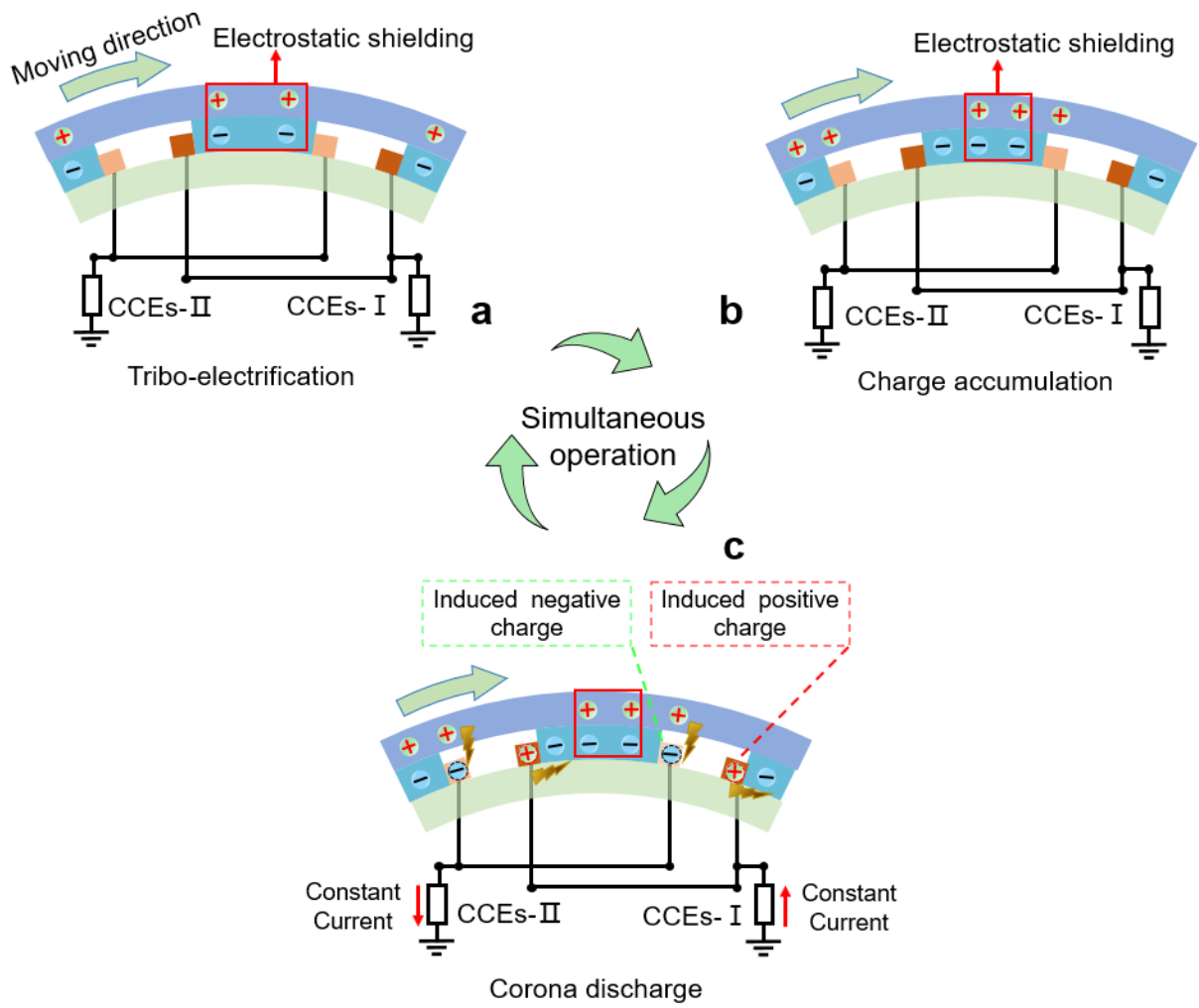**Figure S1.** The more detailed three-dimensional structure diagram of the rolling mode ICC-TENG.

Figure S2. The detailed working mechanism of the ICC-TENG.
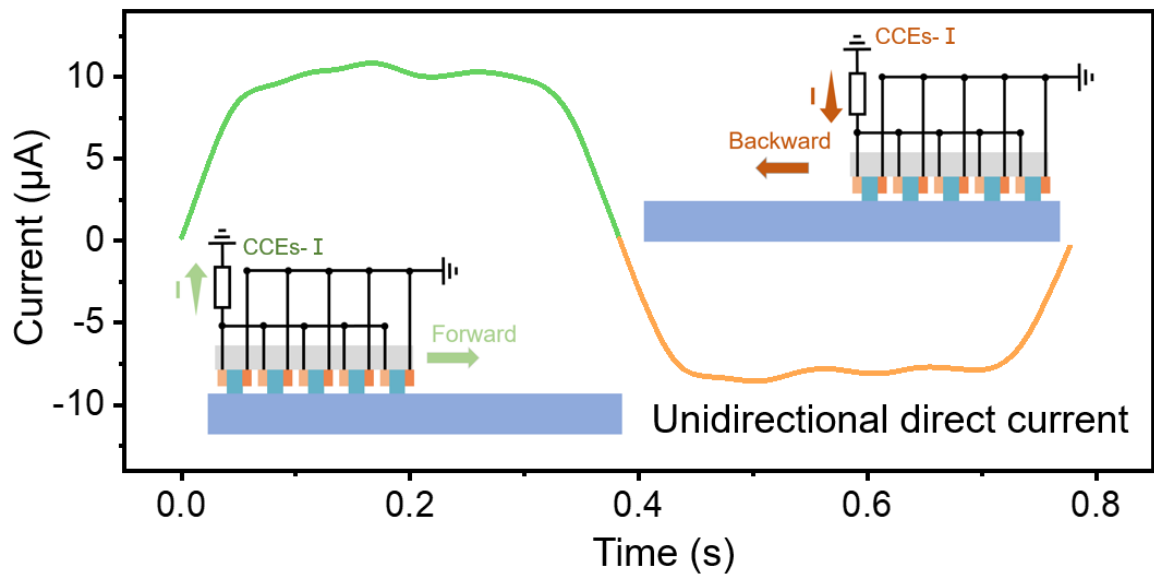
Figures S3. The output current waveform of IDC-TENG during one motion cycle.
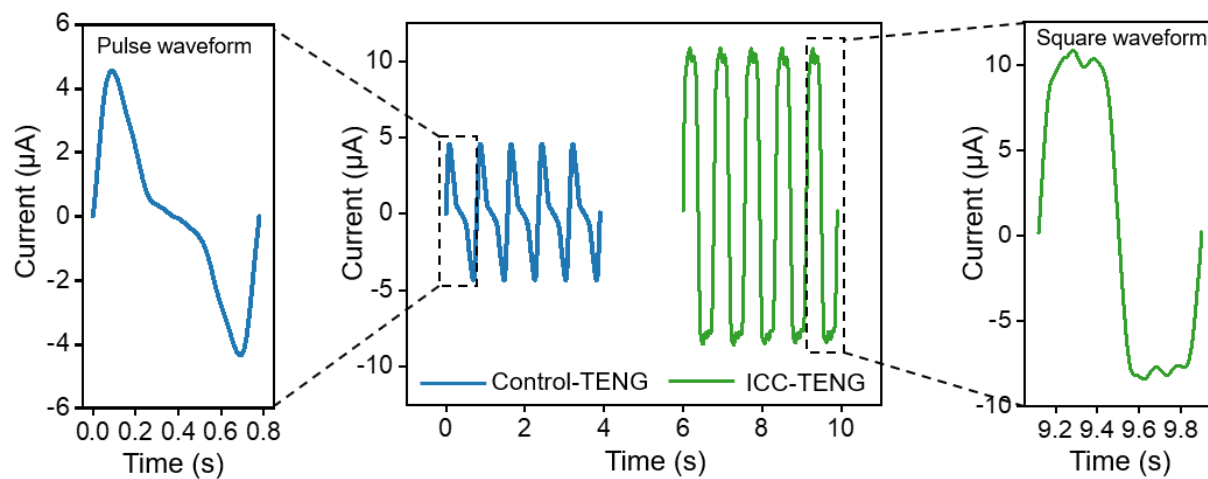
Figure S4. The output current waveform of C-TENG and IDC-TENG.
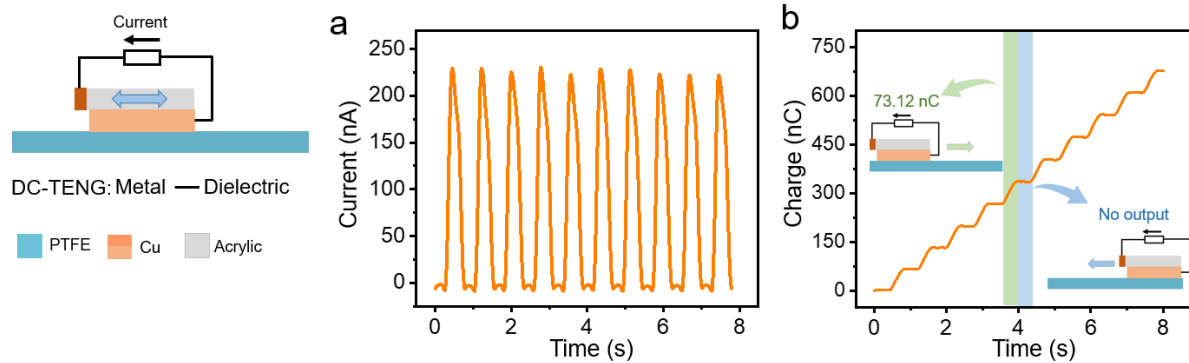
Figure S5. The output current and charge of DC-TENG (Metal-Dielectric).
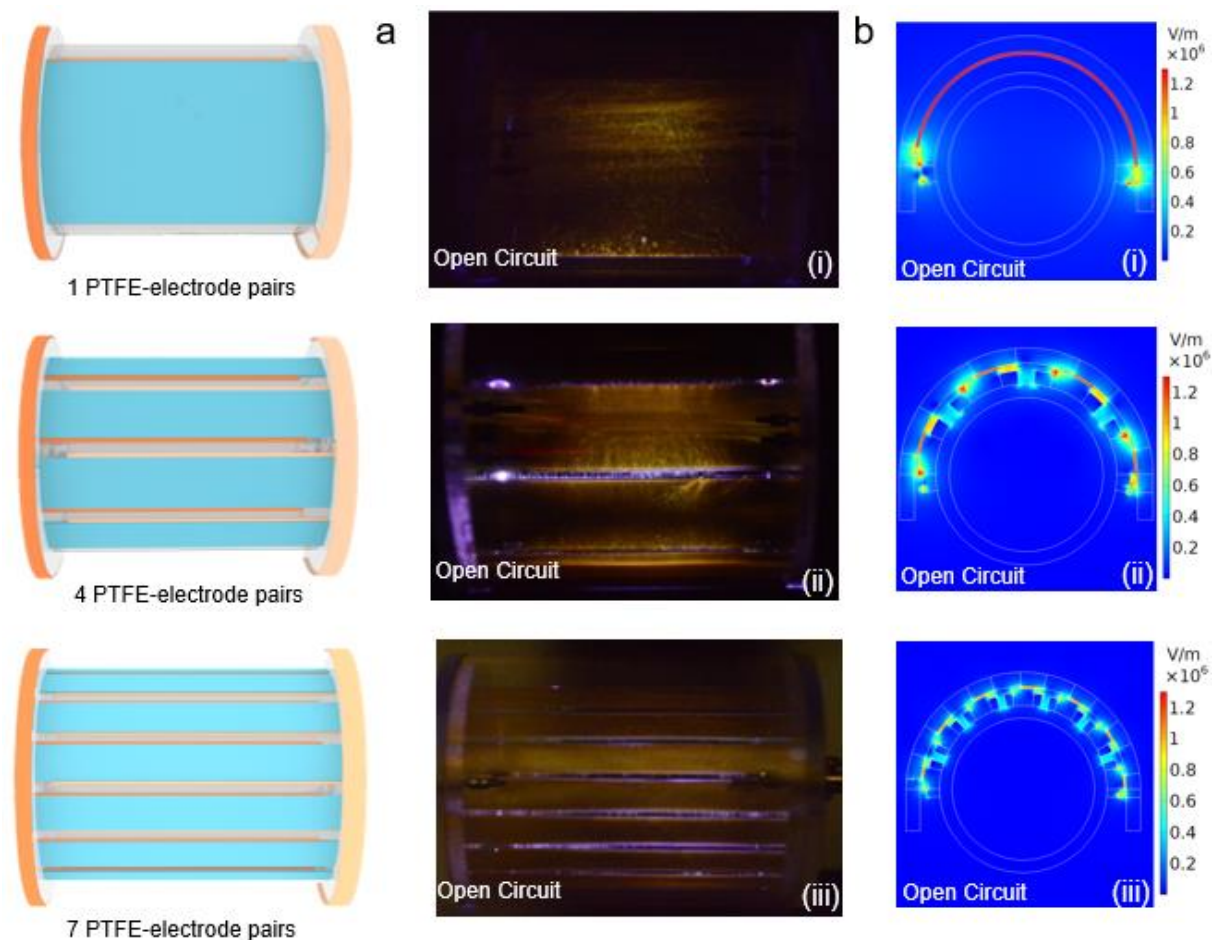
Figure S6. Photograph of corona discharge and electric field distribution of CCEs-I and CCEs-II in the open circuit. (**a**) Photograph of corona discharge and air breakdown glow captured under the open circuit by a digital camera. The corona discharge occurs at the gap between CCEs-I and CCEsII. (**b**) Corresponding electric field distribution of ICC-TENG simulated by COMSOL software under open circuit conditions. (i) 1 PTFE-electrode pairs. (ii) 4 PTFE-electrode pairs. (iii) 7 PTFE-electrode pairs.
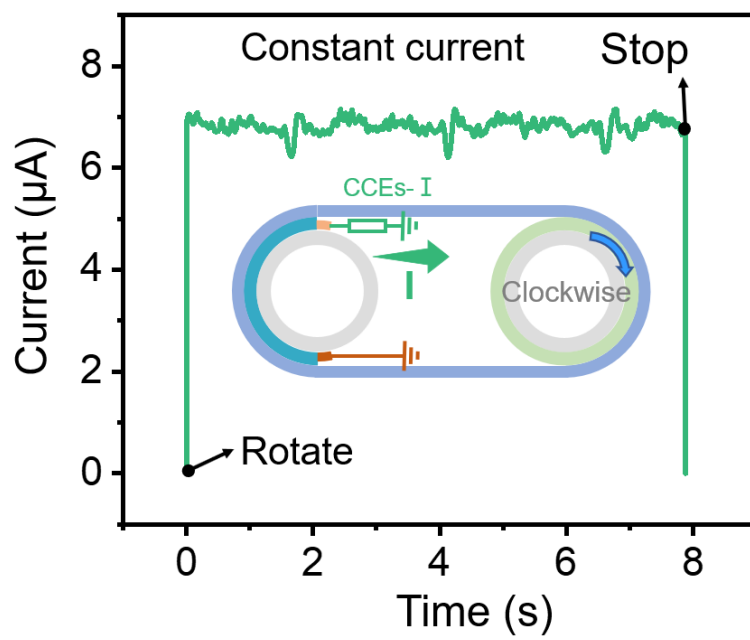
Figures S7. The output current curve of the ICC-TENG when rotating in the clockwise direction.
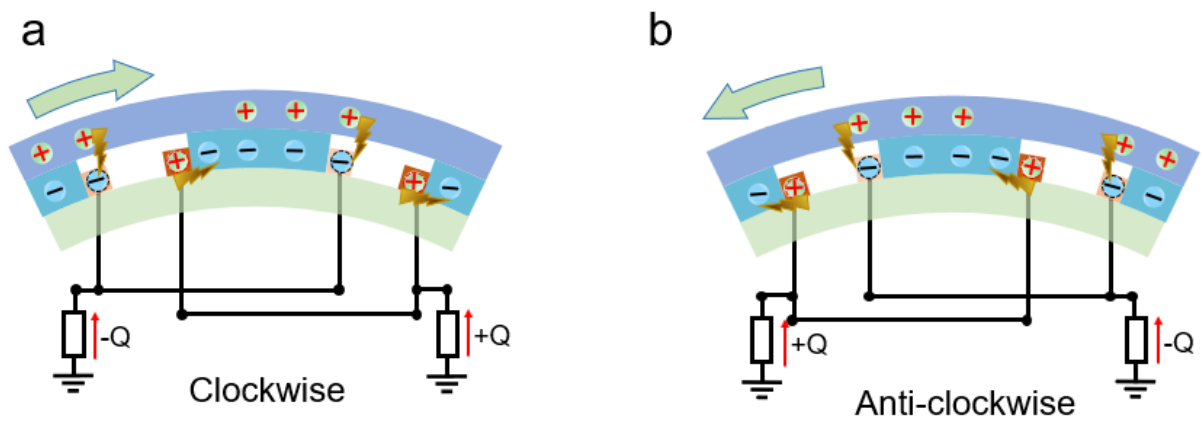
Figure S8. The working mechanism of ICC-TENG in a clockwise rotation or anti-clockwise rotation. **a** Clockwise. **b** Anti-clockwise.
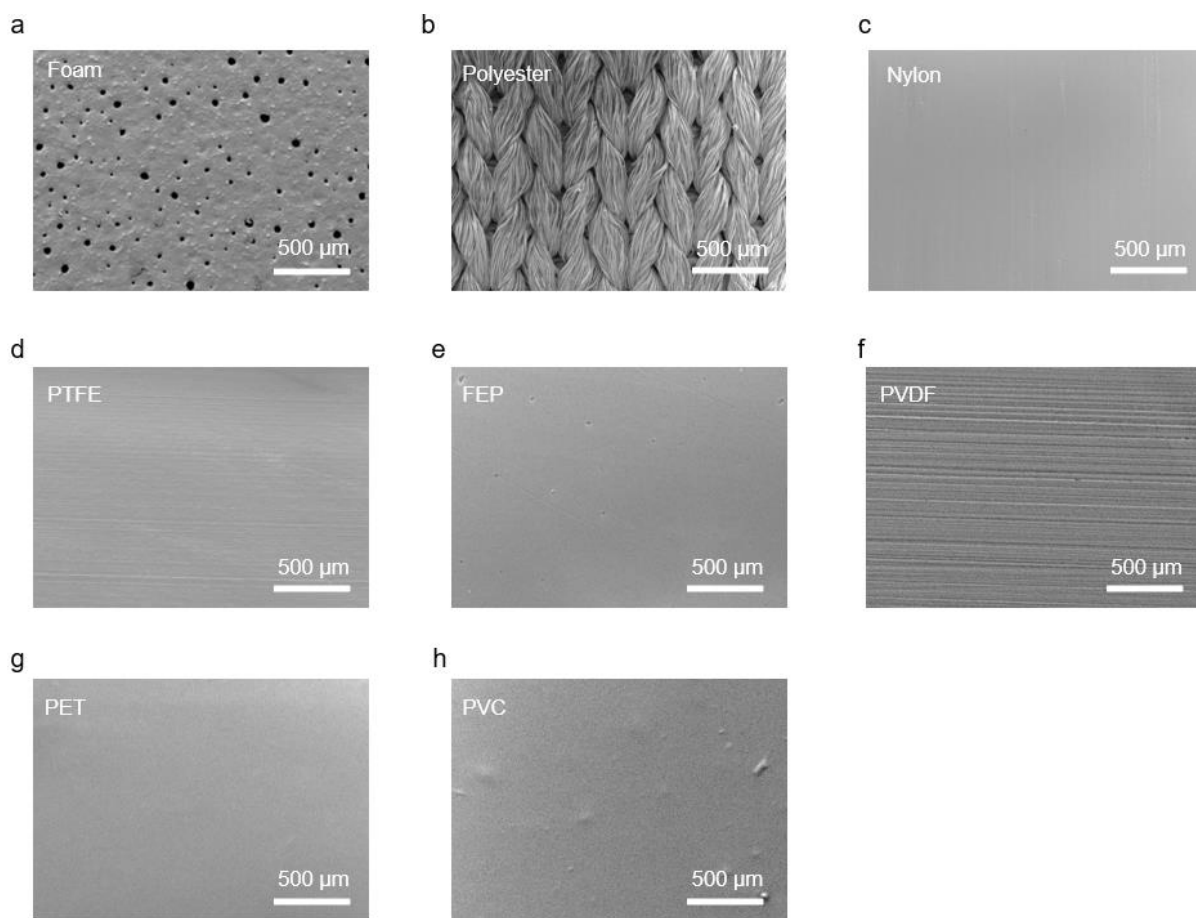
Figure S9. Scanning electron microscopy (SEM) images of all the chosen materials. (a) Foam, (b) Polyester, (c) Nylon, (d) PTFE, (e) FEP, (f) PVDF, (g) PET, and (h) PVC
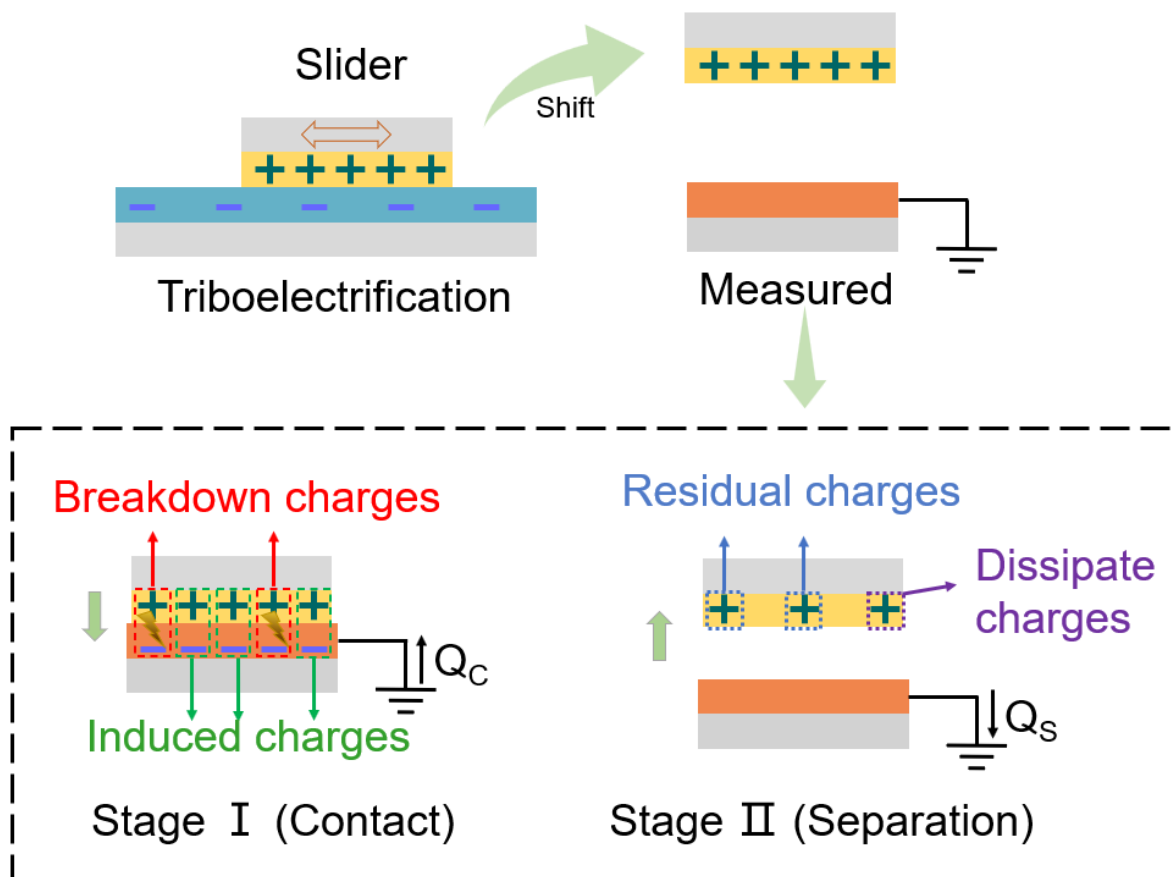
Figure S10. Schematic diagram of measurement of the materials' triboelectric charge states.
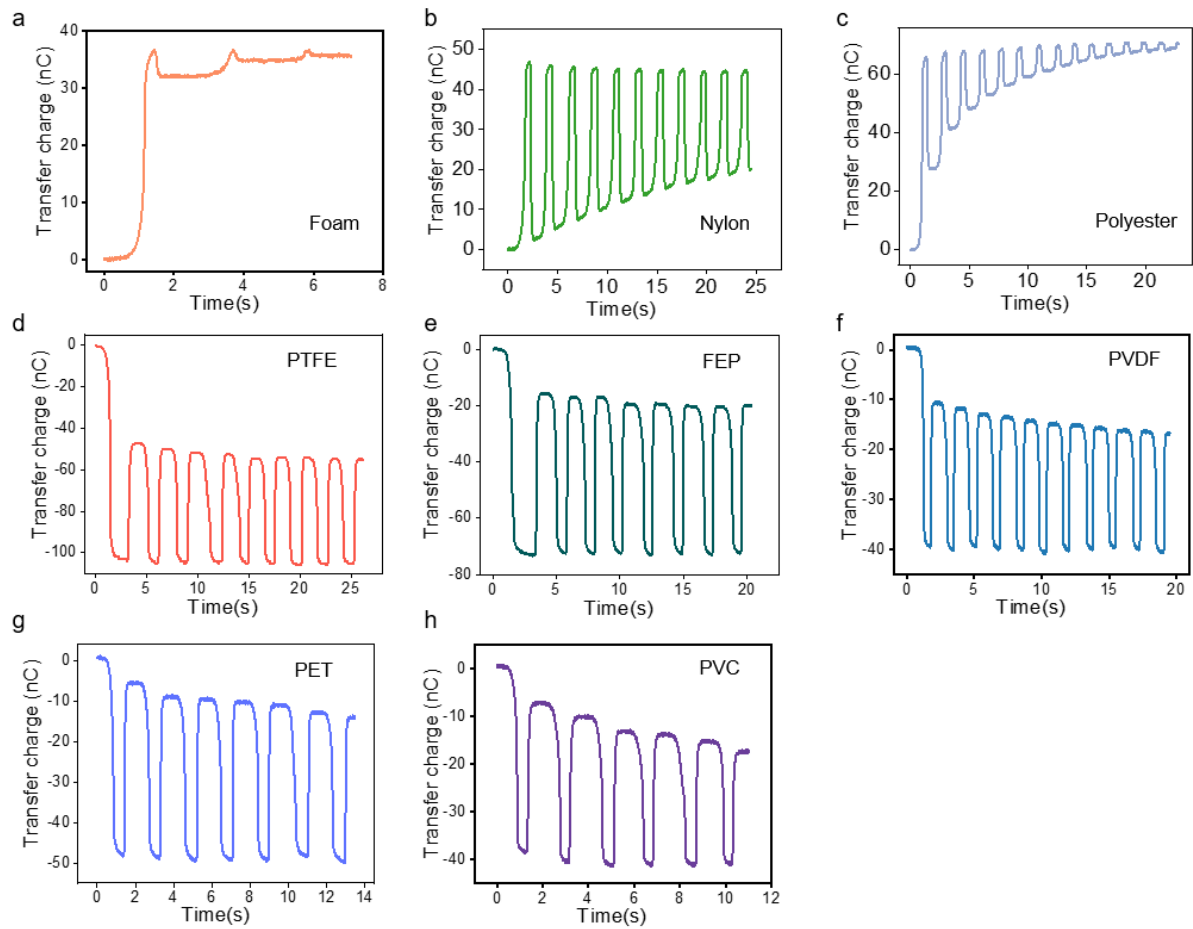
Figure S11. Detailed transferred charge waveform of different materials in the measure of the materials' triboelectric charge states. (a) Foam, (b) Nylon, (c) Polyester, (d) PTFE, (e) FEP, (f) PVDF, (g) PET, and (h) PVC.
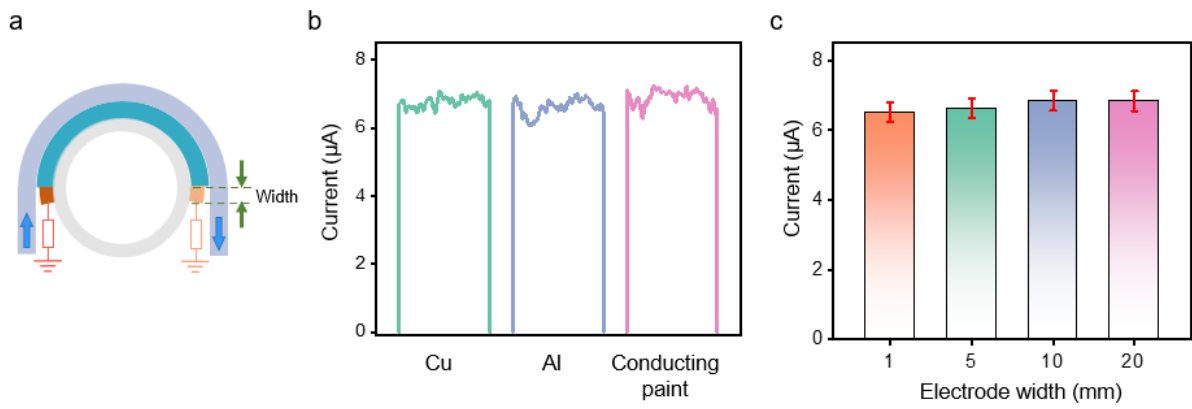
Figure S12. The effect of electrode material on the output performance of ICC-TENG. (a) Schematic diagram of one PTFE-electrode pair. (b) Output current curve with different electrode materials. (c) Output current of ICC-TENG varies with different electrode widths.
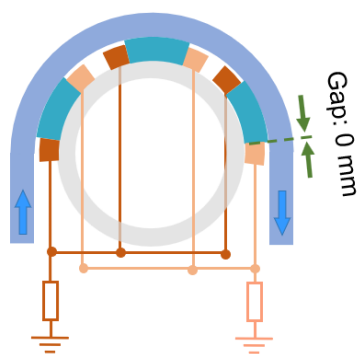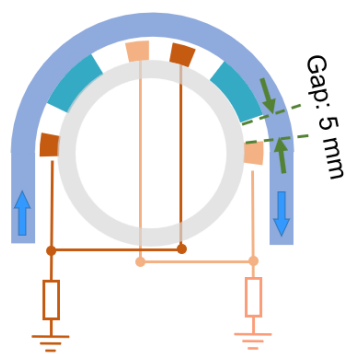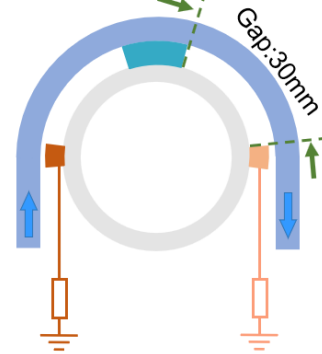
Figure S13. Relationship between the number of integrations and the gap from PTFE to CCEs.
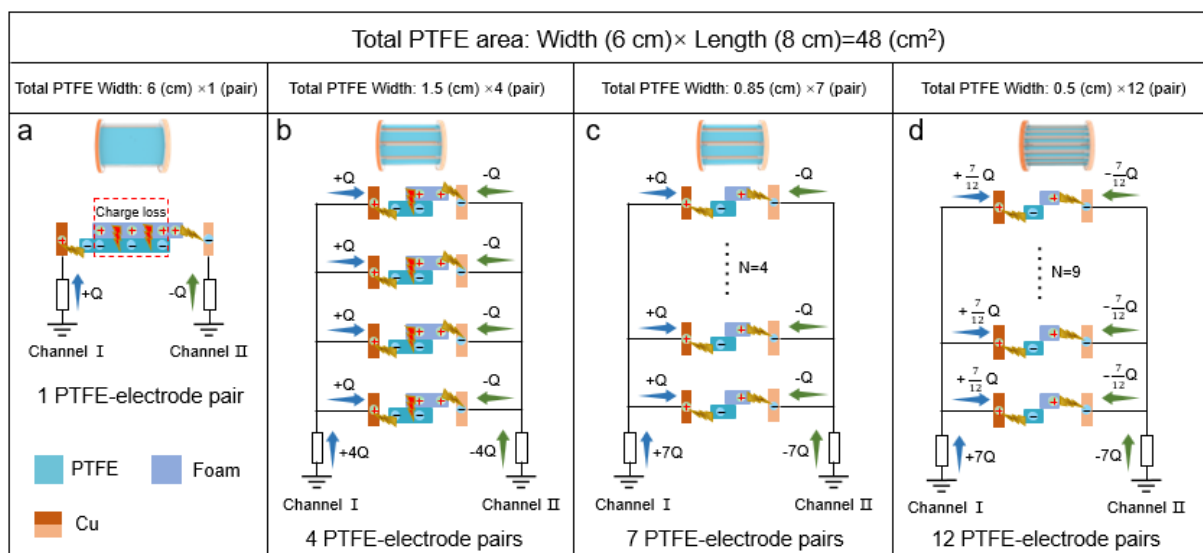
Figure S14. Equivalent physical model of the ICC-TENG for different PTFE-electrode pairs (Equal width of PTFE). (a) 1 PTFE-electrode pair. (b) 4 PTFE-electrode pairs. (c) 7 PTFE-electrode pairs. (d) 12 PTFE-electrode pairs.
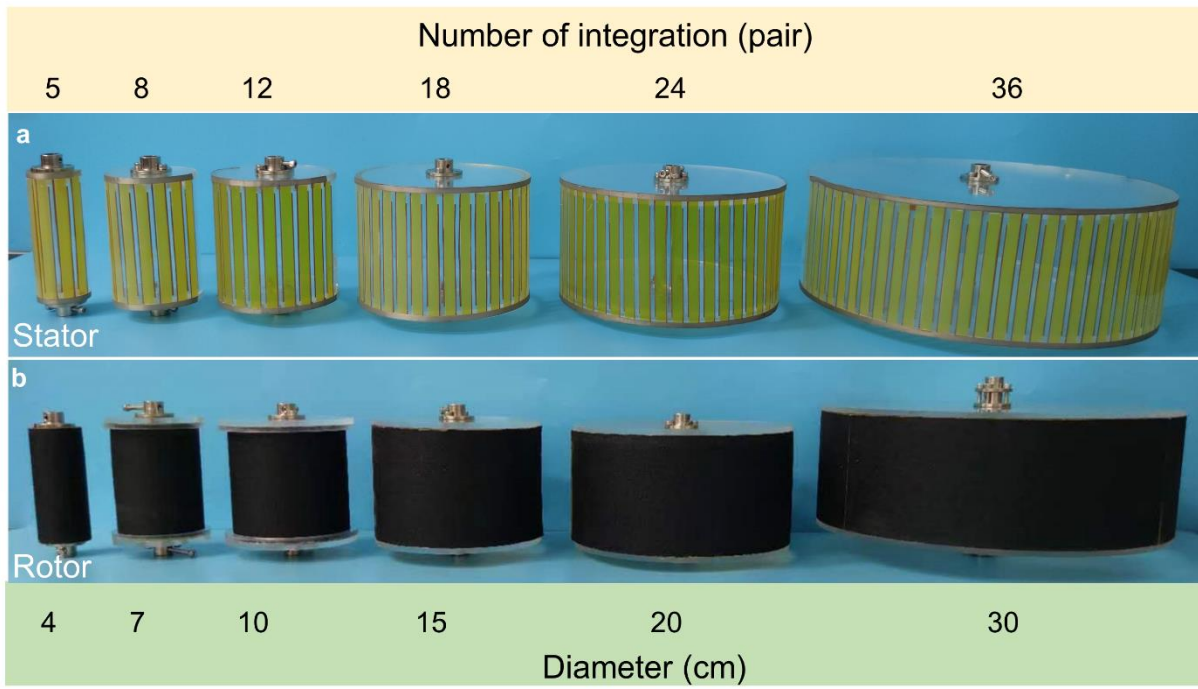
Figure S15. The Optical photographs of the different diameters. (a) rotor. (b) stator.
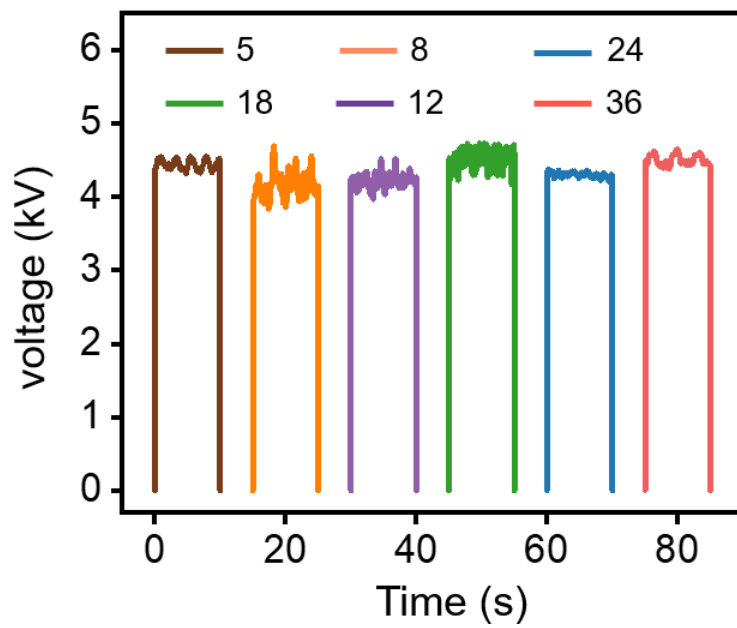
Figure S16. Voltage curves of ICC-TENG with different PTFE-electrode pairs integrated.
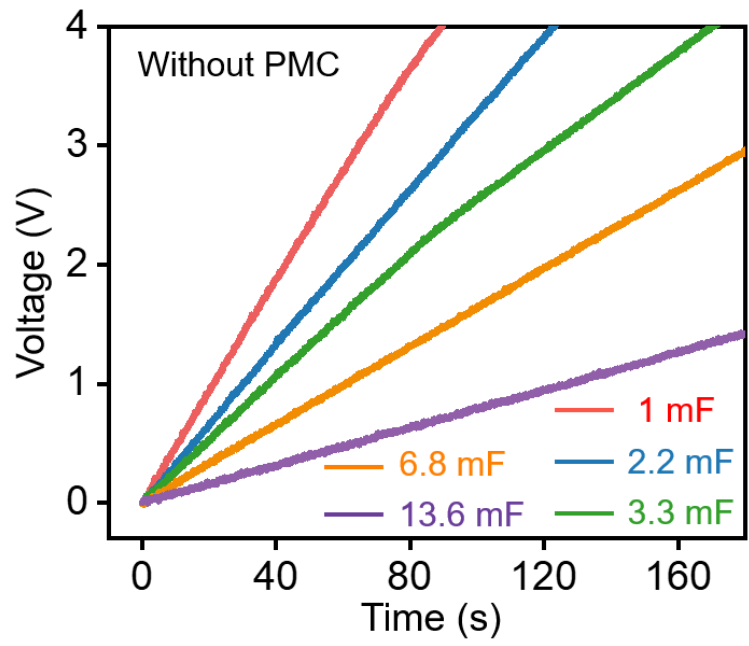
Figure S17. Voltage curves of charging capacitors by ICC-TENG at 30 rpm without PMC.
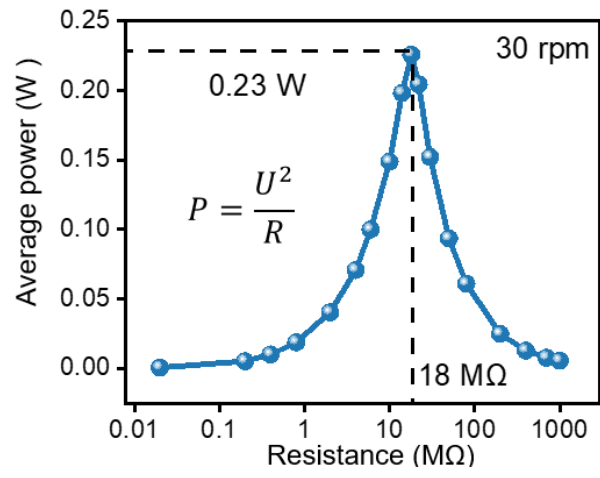
Figure S18. The average power of ICC-TENG under various external loads at 30 rpm.
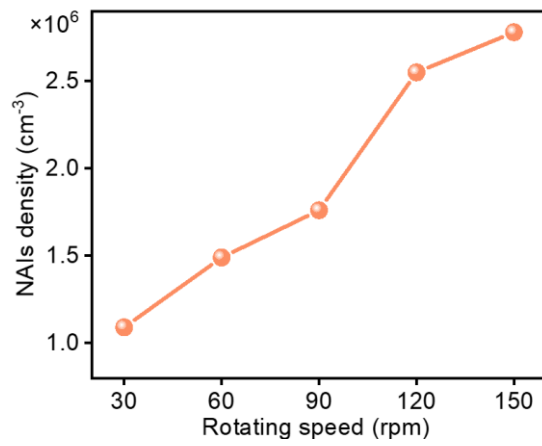
Figure S19. Maximum NAIs density generated by ICC-TENG under various rotating speeds.

Table S1. Comparison of output performance of DC-TENG, AC-TENG, and IDC-TENG.

Type of TENG	Materials	Type	AC/DC	Charge (a cycle)	Peak current
DC-TENG	Metal-Dielectric	Corona discharge	DC (pulse)	73.12+0 (73.12 nC)	4.69 (μA)
AC-TENG	Dielectric-Dielectric	Electrostatic induction	AC (pulse)	0.79+0.79 (1.58 μC)	230.76 (nA)
DC-TENG (This work)	Dielectric-Dielectric	Corona discharge	DC (constant)	3.25+2.66 (5.94 μC)	10.94 (μA)

Table S2. The percentage of the breakdown charge and the residual charge of different materials in the first contact-separation process.

		$Q_C=Q_{total}$	$Q_S=Qr$	$Q_b=Q_C-Q_S$
Electro-positive materials	Foam	Q_1 (+37.5 nC)	14%Q_1	86%Q_1
	Nylon	Q_2 (+46.2 nC)	95%Q_2	5%Q_2
	Polyester	Q_3 (+63.8 nC)	61%	39%
Electro-negative materials	PTFE	Q_4 (-103.6 nC)	54%Q_3	46%Q_3
	FEP	Q_5 (-73.6 nC)	80%Q_5	20%Q_5
	PVDF	Q_6 (-39.4 nC)	75%Q_6	25%Q_6
	PET	Q_7 (-48.4 nC)	90%Q_7	10%Q_7
	PVC	Q_8 (-38.1 nC)	85%Q_8	15%Q_8

Table S3. Systematic comparison of charge density and average power density with the reported works[1-13].

Article	Tribo-materials	AC/DC	Maximum Output Charge rate	Average power density (W m⁻²)	Charge density (mC m-2)
Bai et al. (2020) Adv. Energy Mater[1].	Kapton/Cu	AC	8.8 µC s⁻¹	0.62	0.14
Shan et al. (2021) Energy Environ. Sci[2].	Kapton/Cu/Nylon	AC	3.2 µC s⁻¹	0.63	0.22
Long et al. (2021) Nat. Commun[3].	PTFE/Pa	AC	4.8 µC s⁻¹	0.86	0.071
Chen et al. (2021) Energy Environ. Sci[4].	Rabbit fur/PTFE	AC	12 µC s⁻¹	1.11	0.093
Fu et al. (2021) Adv. Mater[5].	Nylon/FEP	AC	3.54 µC s⁻¹	1.33	0.11
Zhou et al. (2021) Adv. Energy Mater[6].	Kapton/Cu	AC	1.2 µC s⁻¹	0.4	0.31
Yang et al. (2021) Adv. Energy Mater[7].	PVC/Nylon	AC	2.8 µC s⁻¹	0.106	1.328
Liu et al. (2019) Sci. Adv[8].	PTFE/Cu	DC	10 µC s⁻¹	0.35	0.43
Liu et al. (2020) Adv. Mater. Technol[9].	PTFE/Fe	DC	/	0.51	0.74
Li et al. (2022) Energy Environ. Sci[10].	PVC/Cu	DC	15 µC s⁻¹	1.98	0.28
Shan et al. (2022) Adv. Energy Mater[11].	Nylon/PTFE	DC	1.71 µC s⁻¹	3	0.4
Sun et al. (2021) Nona Energy[12]	PTFE/PMMA/ Rubber	DC	4.16 µC s⁻¹	8.08 (3000 rpm)	0.033
Zhao et al. (2021) Nat. Commun[13].	PVC/Cu	DC	4.4 µC s⁻¹	0.2	8.8
This work	PTFE/Foam	DC	360 µC s⁻¹	9.98 (effective area) 5.99 (total area)	10.06

Note S1. The measurement method and theoretical analysis of triboelectric charge state of materials.

Measurement method: The measurement device, which includes a slider, a stator, and a measuring electrode, is shown in **Figure S7**. For measuring electro-positive (negative) materials, the material being measured is attached to the acrylic as the slider, PTFE (foam) is attached to the acrylic surface as the stator, and copper foil is attached on the acrylic surface as the measuring electrode. First, the slider and the stator triboelectrification. Subsequently, the contact-separation process is performed between the slider and the measuring electrode, (**Figure S7** (Stage I and Stage II)) to measure the dynamic output charge of the measuring electrode, the results are presented in **Figure S8.**

Theoretical analysis of triboelectric charge state of materials: Triboelectric charge (Q) is generated on the surface of the slider (material being measured) after triboelectrification between the stator and the slider. At the first contact-separation process. When the slider contacts with the measuring electrode, the measuring electrode induce an equal charge (Q_C). And then part of triboelectric charge on the surface of the material will cause air breakdown (Q_b) with the induced charge on the electrode. In addition, the remaining charge is the surface residual charge (Q_r). The relationship between Q, Q_b, and Q_r can be expressed as[14]:

$$Q = Q_b + Q_r \tag{1}$$

When the slider is separated from the measuring electrode, the surface residual charge is measured (Q_S). In this process, the Q, the Q_b, and the Q_r can be calculated by the following formula.

$$Q = Q_C \tag{2}$$

$$Q_b = Q_C - Q_S \tag{3}$$

$$Q_r = Q_S \tag{4}$$

At the first contact-separation process, the detailed percentage of the breakdown charge and the residual charge of different materials are shown in **Table S2**. The dynamic curve of the surface charge of the triboelectric material can be obtained by repeating the contact separation process described above (**Figure S8**).

Note S2. Influence of the number of PTFE-electrode pairs on the charge output of ICC-TENG under equal width conditions of PTFE**.**

Here, the total width and length of PTFE are defined as W and L. Fixed L unchanged, W is divided into N parts (from 1 to 12) and made into the stator. **Figure S10.** shows the equivalent physical model for 1,4,7,12 PTFE-electrode pairs. The belt speed is defined as v. The CCEs charge-collecting effectively width is defined as E_w. Next, the effect of different numbers of PTFE-electrode pairs on the charge output of ICC-TENG is inferred. When the step motor drives the belt (foam) to rotate, the total charge (Q_{total}) generated by the friction between PTFE and the foam is expressed as

$$Q_{tatol} = \sigma_{PTFE}Lvt \qquad\qquad （5）$$

Taking channel I as an example. **Figure S10** (a) illustrates that the effective charge-collecting width of CCEs for one PTFE-electrode pair is narrower than the actual width of PTFE ($E_w <$ W). Leading to continuous charge accumulation in the middle of PTFE and the formation of a strong electrostatic field that triggers air breakdown and charges loss. The approximate analytical solution of the actual output charge (Q_{OC}) of ICC-TENG can be expressed as

$$Q_{OC} = \frac{E_w}{W}\sigma_{PTFE}Lvt \qquad N = 1 \qquad\qquad (6)$$

The number of CCEs increases proportionally with the number of PTFE-electrode pairs (N), resulting in a corresponding increase in the total effective width for charge-collecting by CCEs (NE_w). Similarly, when $NE_w < W,$ the approximate analytical solution of the Q_{OC} of ICC-TENG can be expressed as

$$Q_{OC} = \frac{NE_w}{W}\sigma_{PTFE}Lvt \qquad N < \frac{W}{E_w} \qquad\qquad (7)$$

When $NE_w > W,$ indicating that the triboelectric charges have been fully collected. At this time, the Q_{OC} of ICC-TENG will not significantly increase with an increasing number of PTFE-electrode pairs. The following equation can be obtained.

$$Q_{OC} = \sigma_{PTFE}Lvt \qquad N > \frac{W}{E_w} \qquad\qquad (8）$$

Therefore, as N increases, the output charge of ICC-TENG first increases and then reaches saturation. When $NE_w = W$, triboelectric charge is just enough to be fully collected.

Note S3. Calculation process of energy conversion efficiency of ICC-TENG.

The energy conversion efficiency can be calculated according to the method described in the previously reported work, the energy conversion efficiency η can be described as follows.

$$\eta = \frac{W_e}{A} \tag{9}$$

$$A = E_F - E_r \tag{10}$$

where W_e is the output electricity in one rotation, A is input mechanical work. E_F is the energy used against the resistance force in one rotation, and E_r is the rotational kinetic energy of the belt. The W_e and E_r can be described as follows.

$$W_e = P_a\,t \tag{11}$$

$$E_r = \frac{1}{2}mv^2 = \frac{1}{2}mR^2\omega^2 \ (v = R\omega) \tag{12}$$

where P_a is the average power and t is the time for one rotation. And m is the mass of the belt, ω is the angular velocity, R is the radius of the rotor.

For one rotation of the rotor, E_F can be calculated as follows.

$$E_F = F \cdot L = 2\pi FR \tag{13}$$

Where the F is resistance force (measured by a dynamometer), L is the sliding distance. Therefore, the energy conversion efficiency η is calculated as follows.

$$\eta = \frac{W_e}{E_F - E_r} = \frac{P_a\,t}{2\pi FR - \frac{1}{2}mR^2\omega^2} \tag{14}$$

For one rotation of the rotating ICC-TENG at 30 rpm. P_a is 230 mW, t is 2 s, m is 0.2 kg, R is 15 cm, ω is π, F is 3.6 N. Therefore, after the above calculation, the energy conversion efficiency η of ICC-TENG is 13.64 %.

Supplementary References

1. Y. Bai, L. Xu, S. Lin, J. Luo, H. Qin, K. Han and Z. L. Wang, *Adv. Energy Mater.*, 2020, 10, 2000605.
2. C. Shan, W. Liu, Z. Wang, X. Pu, W. He, Q. Tang, S. Fu, G. Li, L. Long, H. Guo, J. Sun, A. Liu and C. Hu, *Energy Environ. Sci.*, 2021, 14, 5395-5405.
3. L. Long, W. Liu, Z. Wang, W. He, G. Li, Q. Tang, H. Guo, X. Pu, Y. Liu and C. Hu, *Nat. Commun.*, 2021, 12, 4689.
4. P. Chen, J. An, R. Cheng, S. Shu, A. Berbille, T. Jiang and Z. L. Wang, *Energy Environ. Sci.*, 2021, 14, 4523-4532.
5. S. Fu, W. He, Q. Tang, Z. Wang, W. Liu, Q. Li, C. Shan, L. Long, C. Hu and H. Liu, *Adv. Mater.*, 2022, 34, 2105882.
6. L. Zhou, Y. Gao, D. Liu, L. Liu, Z. Zhao, S. Li, W. Yuan, S. Cui, Z. L. Wang and J. Wang, *Adv. Energy Mater.*, 2021, DOI: 10.1002/aenm.202101958, 2101958.
7. Z. Yang, Y. Yang, H. Wang, F. Liu, Y. Lu, L. Ji, Z. L. Wang and J. Cheng, *Adv. Energy Mater.*, 2021, 11, 2101147.
8. D. Liu, X. Yin, H. Guo, L. Zhou, X. Li, C. Zhang, J. Wang and Z. L. Wang, *Sci. Adv.*, 2019, 5, eaav6437.
9. D. Liu, L. Zhou, S. Li, Z. Zhao, X. Yin, Z. Yi, C. Zhang, X. Li, J. Wang and Z. L. Wang, *Adv. Mater. Technol.*, 2020, 5, 2000289.
10. X. Li, C. Zhang, Y. Gao, Z. Zhao, Y. Hu, O. Yang, L. Liu, L. Zhou, J. Wang and Z. L. Wang, *Energy Environ. Sci.*, 2022, 15, 1334-1345.
11. C. Shan, W. He, H. Wu, S. Fu, Q. Tang, Z. Wang, Y. Du, J. Wang, H. Guo and C. Hu, *Adv. Energy Mater.*, 2022, 12, 2200963.
12. D.-J. Sun, W.-Z. Song, C.-L. Li, T. Chen, D.-S. Zhang, J. Zhang, S. Ramakrishna and Y.-Z. Long, *Nano Energy*, 2022, 101, 107599.
13. Z. Zhao, L. Zhou, S. Li, D. Liu, Y. Li, Y. Gao, Y. Liu, Y. Dai, J. Wang and Z. L. Wang, *Nat. Commun.*, 2021, 12, 4686.
14. D. Liu, L. Zhou, S. Cui, Y. Gao, S. Li, Z. Zhao, Z. Yi, H. Zou, Y. Fan, J. Wang and Z. L. Wang, *Nat. Commun.*, 2022, 13, 6019.